INTERNATIONAL JOURNAL OF ENERGY RESEARCH
Int. J. Energy Res. 2008; **32**:306–317
Published online 11 July 2007 in Wiley InterScience
(www.interscience.wiley.com) DOI: 10.1002/er.1355

Modeling of a geothermal standing column well

E. Abu-Nada*,†, B. Akash, I. Al-Hinti, A. Al-Sarkhi, S. Nijmeh, A. Ibrahim and A. Shishan

Department of Mechanical Engineering, Hashemite University, Zarqa 13115, Jordan

SUMMARY

This paper presents a three-dimensional numerical investigation of a geothermal standing column well (SCW) to carry out heating simulations during January in four selected locations in Jordan. It is shown that the outlet temperature of SCW increases with the depth of the borehole. However, the successful choice of the location is of extreme importance as there is a limit on the outlet temperature that can be achieved at a given location. It is demonstrated that bleeding is generally effective in increasing the outlet temperature. An optimum range of bleed rate exists around 12–13%. Also, bleeding is more effective in achieving higher outlet temperatures when used in locations with higher soil porosity.

KEY WORDS: geothermal energy; standing column well; Jordan

1. INTRODUCTION

Ground source heat pump (GSHP) uses either the ground as a heat source or sink. The system allows the heat pump to extract or reject heat from and to the ground. GSHPs are either open- or closed-loop systems. Open-loop GSHP structure uses a pump to circulate groundwater through the heat pump heat exchanger. Closed-loop GSHP system employs a pump to circulate fluid through pipes buried horizontally or inserted vertically into boreholes in the ground [1–3]. The third type is a groundwater heat pump system that uses groundwater drawn from wells in a semi-open loop arrangement which is commonly known as 'standing column well' (SCW) system [4]. The system allows water to be circulated between the well and the heat pump as shown in Figure 1. During peak demand periods, the performance can be enhanced by water bleed. The system can 'bleed' or reject part of the water from the heat pump. However, similar amount of the bleed water is replaced into the well from the surrounding aquifer through uniformly slotted casing. The SCW system received attention because of its lower installation and running costs. Also, it has

*Correspondence to: E. Abu-Nada, Department of Mechanical Engineering, Hashemite University, Zarqa 13115, Jordan.
†E-mail: eiyad@hu.edu.jo

Contract/grant sponsor: Abdul Hameed Shoman Fund
Contract/grant sponsor: Hashemite University

Received 11 January 2007
Revised 20 May 2007
Accepted 1 June 2007

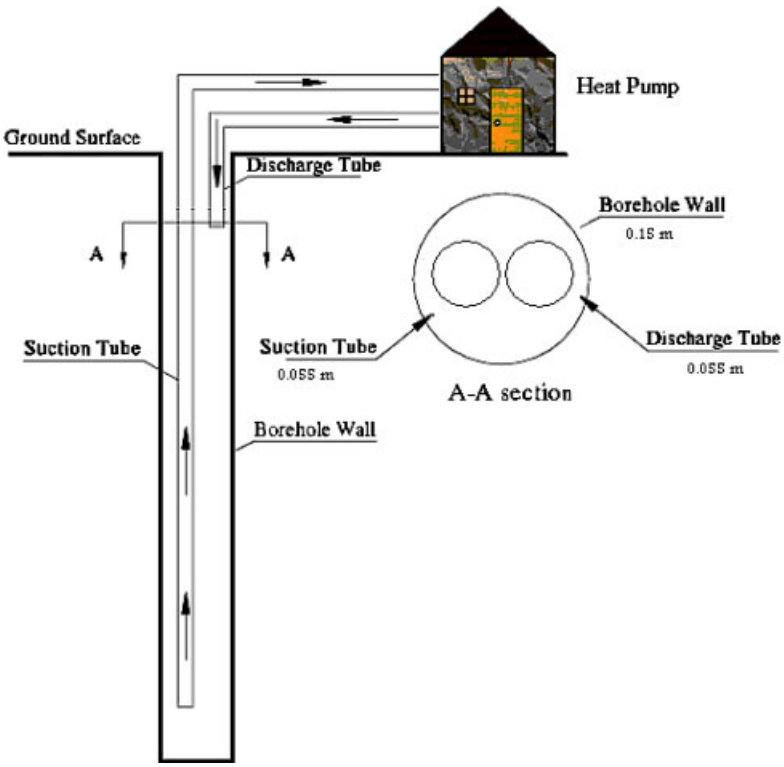

Figure 1. Schematic diagram of the SCW.

very important applications in commercial and industrial designs since it gives stable temperatures, especially, in the regions of higher heating loads. According to Orio [5], the improved overall performance of the geothermal heat pump in the areas of the proper geological and hydrological parameters is the main reason for the latest increases in the research work on the SCW.

It is important to point out that Jordan has enormous geothermal energy resources in many parts of the country in the form of thermal underground hot water (wells and thermal springs) but its use is, exclusively, limited to therapeutic application. At the same time, Jordan has a serious energy problem due to full dependency on the imported oil, which places a huge burden on its budget. The annual consumption of heavy fuel oil, diesel fuel, and kerosene adds up to more than 70% of the entire quantity of all fuel consumed, based on energy equivalent value [6]. Therefore, enhancing new and renewable energy utilization in Jordan has become necessary. Currently, renewable energy accounts for only 2% of energy use, mostly in the form of solar water heating systems [7]. Other applications include solar ponds, small wind farms for electric power generation, water pumping by windmills and photovoltaic cells for urban use of electricity [8, 9]. It was reported that more than 60% of the energy consumed in the residential sector is used in space heating. This accounts to about 14% of annual national energy demand [10]. Therefore, the country needs to consider geothermal energy as an energy source. Thermal springs form the main source of geothermal energy in Jordan with temperature range of 20–62°C. These springs are distributed along the eastern escarpment of the Jordan Valley and Dead Sea Basin (200 km). About 100 thermal wells drilled for water in Dead Sea–Rift Valley, Area of Azraq Basin and Risha (Northeast Jordan), the area south of Queen Alia

DOI: 10.1002/er

Airport have low to intermediate water temperatures. Sunna' [11] summarized and identified these thermal wells and springs.

Extensive research in literature focused on SCW systems and their applications. For example, transient heat and mass transfer was investigated experimentally in SCW system in two wells [12]. In another study, a simplified mathematical model was derived to analyze the coupled thermo-hydraulic energy transfer by conduction and convection in an aquifer surrounding a thermal well [13]. Rees *et al.* [4] modeled SCW numerically. The model was used for a parametric study to find out the effect of the most important design parameters on the well performance. Their results showed that the groundwater percentage of bleed is the most important parameter for improving the well performance. Their work used a two-dimensional model in the radial–axial directions, to study fluid and heat transfer in the SCW. It used finite volume method in calculating ground water flow and heat transfer rates over a one-year operating period. Further simplified one-dimensional models were also proposed by Deng *et al.* [14] and Abu-Nada *et al.* [15]. Although the previous models give approximate estimates for the transport quantities in SCW, they neglect three-dimensional effects encountered in SCW system [16]. In fact, heat and fluid flows in SCW are three-dimensional due to the complex processes encountered in the SCW geometry, especially if mass bleed is encountered. Also, the huge difference in geometrical scale between the borehole diameter ($D = 0.15$ m) and surrounding porous medium far away diameter (130 m) and the depth of the borehole ($L = 50$ m), requires an accurate prediction of transport quantities at the interface between the borehole and surrounding porous medium. The present work provides modeling for a SCW to predict fluid temperature (the inlet fluid temperature to the heat pump). Besides, it helps in the determination of the necessary well depth per given heating load. The influence of bleed rate on SCW performance is also examined. Figure 1 shows a schematic diagram for the SCW connected to a heat pump. The SCW consists of a borehole filled with water and a surrounding porous medium (the ground). The surrounding porous medium is considered as a geothermal reservoir, which supplies heat to the SCW. Theoretically, the size of this reservoir is infinity. However, for simulation purposes the far-field radius is taken equal to 65 m. This value was consistent with previous work of different researchers [4]. The borehole radius is taken equal to 75 mm. Thus, the ratio of far-field radius to the borehole radius is large enough to ensure that the surrounding porous medium resembles a geothermal reservoir. The depth of the borehole is taken equal to 50 m. The length of the suction tube is equal to 48 m, whereas the length of the discharge tube is equal to 2 m.

2. GOVERNING EQUATIONS

The flow in porous media is assumed steady, incompressible with constant fluid properties. The continuity, momentum for fluid and heat flow in porous media (in r, θ, and z directions, respectively) and energy equations are given as [17, 18]:

$$\frac{1}{r}\frac{\partial rv}{\partial r}+\frac{1}{r}w\frac{\partial w}{\partial \theta}+u\frac{\partial u}{\partial z}=0 \tag{1}$$

$$\begin{aligned}\frac{\rho_f}{\epsilon^2}\left(v\frac{\partial v}{\partial r}+\frac{1}{r}w\frac{\partial v}{\partial \theta}+u\frac{\partial u}{\partial z}\right)-\frac{\rho_f}{\epsilon^2}\frac{w^2}{r}\\ =-\frac{\partial p}{\partial r}+\frac{\mu}{\epsilon}\left(\frac{1}{r}\frac{\partial}{\partial r}\left(r\frac{\partial v}{\partial r}\right)+\frac{1}{r}\frac{\partial^2 v}{\partial \theta^2}+\frac{\partial^2 v}{\partial z^2}\right)\\ -\frac{\mu}{\epsilon}\frac{v}{r^2}-\frac{2\mu}{\epsilon}\frac{1}{r^2}\frac{\partial w}{\partial \theta}+S_r\end{aligned} \tag{2}$$

$$\begin{aligned}\frac{\rho_f}{\epsilon^2}\left(v\frac{\partial w}{\partial r}+\frac{1}{r}w\frac{\partial w}{\partial \theta}+u\frac{\partial w}{\partial z}\right)-\frac{\rho_f}{\epsilon^2}\frac{vw}{r}\\ =-\frac{1}{r}\frac{\partial p}{\partial \theta}+\frac{\mu}{\epsilon}\left(\frac{1}{r}\frac{\partial}{\partial r}\left(r\frac{\partial w}{\partial r}\right)+\frac{1}{r}\frac{\partial^2 w}{\partial \theta^2}+\frac{\partial^2 w}{\partial z^2}\right)\\ -\frac{\mu}{\epsilon}\frac{w}{r^2}+\frac{2\mu}{\epsilon}\frac{1}{r^2}\frac{\partial v}{\partial \theta}+S_\theta\end{aligned} \tag{3}$$

DOI: 10.1002/er

$$\frac{\rho_f}{\epsilon^2}\left(v\frac{\partial u}{\partial r}+\frac{1}{r}w\frac{\partial u}{\partial \theta}+u\frac{\partial u}{\partial z}\right) = -\frac{\partial p}{\partial z}+\frac{\mu}{\epsilon}\left(\frac{1}{r}\frac{\partial}{\partial r}\left(r\frac{\partial u}{\partial r}\right)+\frac{1}{r}\frac{\partial^2 u}{\partial \theta^2}+\frac{\partial^2 u}{\partial z^2}\right) - \frac{\mu}{\epsilon}\frac{w}{r^2}+\frac{2\mu}{\epsilon}\frac{1}{r^2}\frac{\partial v}{\partial \theta}+S_\theta \quad (4)$$

$$\left(v\frac{\partial T}{\partial r}+\frac{1}{r}w\frac{\partial T}{\partial \theta}+u\frac{\partial T}{\partial z}\right) = \left(\frac{1}{r}\frac{\partial}{\partial r}\left(r\alpha_{\text{eff}}\frac{\partial T}{\partial r}\right)+\frac{1}{r}\frac{\partial^2(\alpha_{\text{eff}}T)}{\partial \theta^2}+\frac{\partial^2(\alpha_{\text{eff}}T)}{\partial z^2}\right) \quad (5)$$

Equations (2)–(5) can be written in a general transport equation as

$$\rho_f\frac{\partial}{\partial r}\left(r\left(v\varphi-\mu\epsilon\frac{\partial \varphi}{\partial r}\right)\right)+\rho_f\frac{\partial}{\partial \theta}\left(\frac{1}{r}\left(r\omega\varphi-\mu\epsilon\frac{\partial \varphi}{\partial \theta}\right)\right) + \rho_f\frac{\partial}{\partial z}\left(r\left(u\varphi-\mu\epsilon\frac{\partial \varphi}{\partial z}\right)\right)=S \quad (6)$$

where S is the source term and is given as

$$S_r=\left(\frac{\mu}{K}+\frac{C_F\sqrt{v^2+w^2+u^2}}{\epsilon\sqrt{K\epsilon}}\right)v \quad (7)$$

$$S_\theta=\left(\frac{\mu}{K}+\frac{C_F\sqrt{v^2+w^2+u^2}}{\epsilon\sqrt{K\epsilon}}\right)w \quad (8)$$

$$S_z=\left(\frac{\mu}{K}+\frac{C_F\sqrt{v^2+w^2+u^2}}{\epsilon\sqrt{K\epsilon}}\right)u \quad (9)$$

$$S_T=0 \quad (10)$$

The last terms in Equations (7)–(9) represent the Darcy and Forchheimer terms, respectively. However, the Brinkman term appears in Equation (6) as the diffusion term. The porosity, ϵ, is related to permeability (K) through the Ergun's relation [18]

$$K=\frac{1}{150}\frac{\epsilon^3 d_p^2}{(1-\epsilon)^2} \quad (11)$$

The simulation is done by solving the full three-dimensional Navier–Stokes equations and energy equation in the porous medium and inside the borehole. The model considered the porous medium as homogeneous and isotropic. The above equations are applied throughout the porous medium surrounding the borehole. However, for the water inside the borehole (clear fluid flow) the same governing equations are applicable, but the value of porosity is set to unity. In this case, the resistance associated with the porous media vanishes and accordingly the Darcy and the Forchheimer terms vanish automatically.

The use of three-dimensional full Navier–Stokes equations in the current model has many advantages. It mimics the three-dimensional nature of the flow geometry under study. The non-symmetrical location of suction tube and discharge tube creates a three-dimensional heat and flow effects. Also, the three-dimensional formulation is suited for flow characterized as turbulent flow for high value of Reynolds number. Although the current simulation assumes laminar flow, the extension of the current model to turbulent flow should be easy by using the three-dimensional formulation.

3. BOUNDARY CONDITIONS

In order to solve the governing equations (i.e. Equations (6)–(10)), a set of boundary conditions has to be determined. The boundary conditions are applied for the city of *Salt*. However, further analysis for other places such as *Ghor-Safi*, *Zarqa*, and *Shoubak* will also be carried out in the discussion of Results section.

3.1. Far-field boundary condition

Temperature distribution in the ground is a function of time (during the year) and depth below the ground level. The temperature profile is given by the following correlation [19]:

$$T=T_m-T_a\exp\left(-\ell\left(\frac{\pi}{365\alpha_s}\right)^{0.5}\right) \times\cos\left(\frac{2\pi}{365}\left(t-t_{cd}-\frac{\ell}{2}\left(\frac{\pi}{365\alpha_s}\right)^{0.5}\right)\right) \quad (12)$$

Figure 2 shows the underground temperature distributions for a couple of locations in Jordan

DOI: 10.1002/er

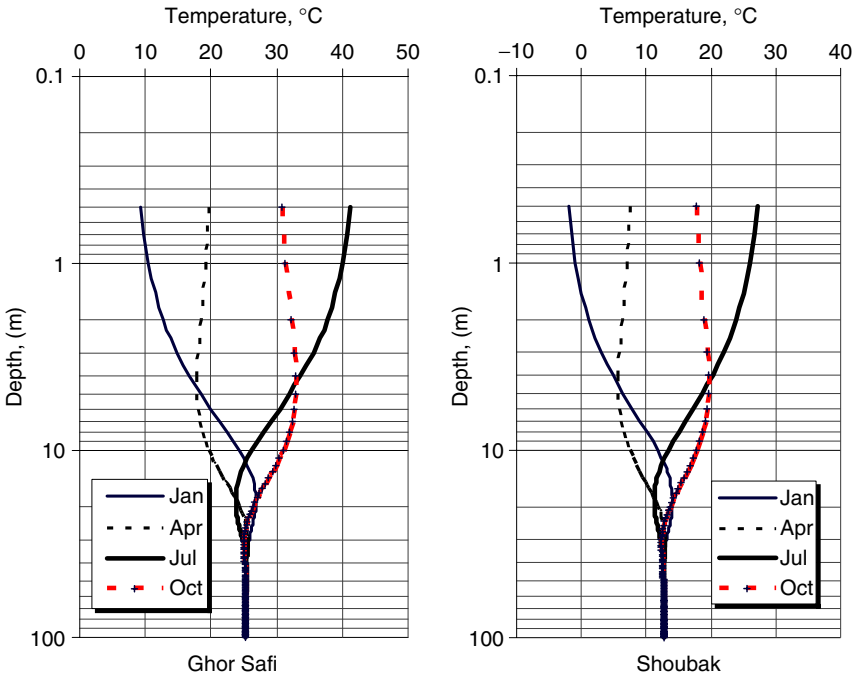

Figure 2. Underground temperature distribution for Ghor-Safi and Shoubak.

(*Ghor Safi* and *Shoubak*). A similar temperature distribution can also be presented for another location (the city of *Salt*). By using the above equation, the bottom and top surface temperatures of the SCW (computational domain), in *Salt* during the month of January, are fixed at 1 and 14.9°C, respectively.

The velocity boundary condition on the far-field radius is taken as the no-flow boundary condition:

$$u = v = w = 0 \tag{13}$$

3.2. Borehole boundary condition

Fluid flow is mainly directed inside the borehole to increase the water inlet temperature to the heat pump. In this operation, cold water enters the well *via* the discharge tube and then returns at higher temperature to the heat pump through the suction pipe, see Figure 1. It is worth mentioning that the borehole was assumed to be full of water. The boundary conditions that are applied to the fluid domain in the borehole are as follows:

3.2.1. At the inlet. At the inlet of the discharge tube, the inlet temperature is taken as the discharge temperature from the heat pump:

$$T_{\text{inlet}} = 5°\text{C} \tag{14}$$

The velocity at the inlet of the discharge tube is determined from the mass flow rate leaving the heat pump, which is estimated as

$$u_{\text{inlet}} = \frac{\dot{m}_{\text{inlet}}}{A_{\text{d}}} \tag{15}$$

where A_{d} is the area of the discharge tube. Note that both v and w are set to zero at inlet, which means that the flow is considered to flow straight downward the borehole. Also, the velocity at the circumference of the borehole surface is set equal to zero. The top surface of the borehole (well head) is considered impermeable where no cross-flow can occur, which means a no-flow boundary condition is applied on the borehole well head.

DOI: 10.1002/er

3.2.2. At the outlet. The outlet boundary condition is specified by assuming that the static gauge pressure at the discharge pipe outlet is equal to zero

$$P_{\text{outlet}} = 0 \tag{16}$$

3.2.3. Walls of the suction and discharge tube. The walls of discharge and suction tubes are assumed to be adiabatic surfaces and are impermeable. This means that the heat flux is set equal to zero and a no-slip velocity boundary condition is imposed on the walls.

3.2.4. Walls of the borehole. To couple the borehole model and the surrounding porous medium model, the heat flux applied to the borehole wall from the surrounding porous medium is calculated. Then, this heat flux is used as a boundary condition at the borehole wall in the finite volume formulation. In turn, this calculates the borehole wall temperature and passes this back to the borehole model.

3.3. Boundary conditions due to bleed rate

Part of the water that exits from the heat pump is discharged around the borehole. This is known as bleed. The bleed percentage is defined as the ratio of water poured into the porous medium around the borehole to the total water that exits from the heat pump. The water bleed is assumed homogenous around the borehole. In the present analysis, bleed is defined in terms of velocity and temperature boundary condition. The velocity boundary condition is specified by dividing the bleed flow rate by the effective area where the bleed is taking place. This area is taken as the area around the borehole with a radius equal to 3 m around the borehole center line. Thus, the bleed velocity is given as

$$V_{\text{b}} = \frac{\dot{m}_{\text{bleed}}}{(\pi d_{\text{b}}^2/4)} \tag{17}$$

where d_{b} is equal to 3 m. The temperature at bleed area is assumed equal to the outlet temperature from the heat pump, i.e. equal to 5°C. The borehole was considered permeable when bleed rate exist.

4. NUMERICAL IMPLEMENTATION

Equations (6)–(10) with the corresponding mentioned boundary conditions are solved using the finite volume. The computational flow domain is decomposed into a set of non-overlapping control volumes surrounding a grid node, as shown by the dotted lines in Figure 3. A staggered grid arrangement is used where the velocity components are evaluated at the faces of the control volume (the dashed volume in Figure 3). The faces of the control volume are defined by the lower case letters in Figure 3 (i.e. e, w, s, n, b, and t). However, other scalar quantities such as temperature and pressure are evaluated at the center of the control volume. The governing equations are integrated over each control volume and are discretized in terms of the values at a set of nodes defining the computational mesh (E, W, N, S, B, and T as shown in Figure 3). The SIMPLE algorithm is used as the computational algorithm [20]. For full details of the method see References [20, 21]. It is worth mentioning that a pressure correction scheme is used by using the continuity equation. The continuity equation is expressed as a Poisson equation for pressure correction for the flow field. The full detail of this procedure is also given by Patankar [20].

The diffusion term in Equation (6) is approximated by second-order central difference which gives a very stable solution. However, a second-order

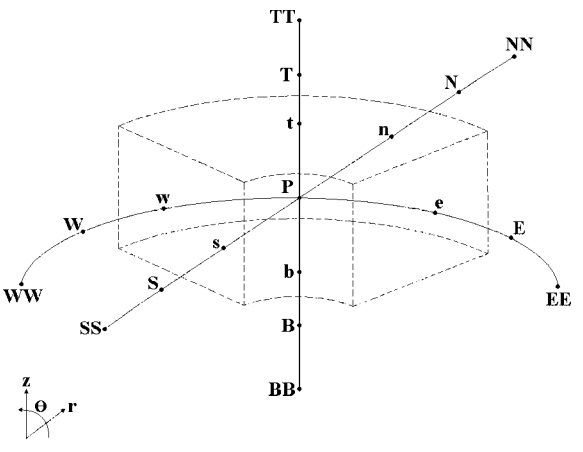

Figure 3. Computational control volume.

DOI: 10.1002/er

upwind differencing scheme is adopted for the convective terms. This scheme uses second-order extrapolation of two upwind neighbors to determine any transport quantity φ. The second-order upwind term is written in the following general form for the angular directions:

$$\left.\frac{\partial(w\varphi)}{\partial\theta}\right|_{\mathrm{P}} = \frac{1}{2\Delta\theta}(3w_{\mathrm{P}}\,\varphi_{\mathrm{P}} - 4w_{\mathrm{W}}\varphi_{\mathrm{W}} + 3w_{\mathrm{WW}}\varphi_{\mathrm{WW}}) \quad \text{for } w>0 \tag{18}$$

$$\left.\frac{\partial(w\varphi)}{\partial x}\right|_{\mathrm{P}} = \frac{1}{2\Delta x}(-w_{\mathrm{EE}}\,\varphi_{\mathrm{EE}} + 4w_{\mathrm{E}}\varphi_{\mathrm{E}} - 3w_{\mathrm{P}}\varphi_{\mathrm{P}}) \quad \text{for } w<0 \tag{19}$$

Similar expressions could be written for the r and z directions. Figure 3 shows the control volume with the symbols used in Equations (18) and (19).

A fine grid is used in the borehole and its outer radius to resolve steep temperature gradients, while a coarser grid is used at far-field radius. This is done using a grid stretching technique that results in considerable savings in terms of the grid size and thus in computational time. The grid stretching method is done by transforming the uniform spacing grid points, in the r-direction, into a non-uniform grid, by using the following transformation [22]:

$$r = \gamma\left(1 + \frac{\sinh[\beta(\mathrm{RU} - A)]}{\sinh(\beta A)}\right) \tag{20}$$

where A is a constant given by [23]:

$$A = \frac{1}{2\beta}\ln\left[\frac{1 + (\mathrm{e}^{\beta} - 1)(\gamma/R_{\infty})}{1 + (\mathrm{e}^{-\beta} - 1)(\gamma/R_{\infty})}\right] \tag{21}$$

The governing equations are integrated over the control volume $\Delta r\Delta\theta\Delta z$; for details of integration, see Versteeg and Malalasekera [21]. The final discretized algebraic finite volume equations are written into the following form:

$$-a_{\mathrm{E}}\varphi_{\mathrm{E}} - a_{\mathrm{W}}\varphi_{\mathrm{W}} + a_{\mathrm{P}}\varphi_{\mathrm{P}} = a_{\mathrm{N}}\varphi_{\mathrm{N}} + a_{\mathrm{S}}\varphi_{\mathrm{S}} + a_{\mathrm{B}}\varphi_{\mathrm{B}} + a_{\mathrm{T}}\varphi_{\mathrm{T}} + b \tag{22}$$

where P is the center of cell location and W, E, N, S, B, and T denote other locations: west, east, north, south, bottom, and top faces of the control, respectively. The symbol φ in Equation (22) holds for u, v, w, or T and symbol b resembles the source term. The resulting algebraic equations are solved with tri-diagonal matrix algorithm (Thomas algorithm) with the line-by-line relaxation technique. For each two-dimensional plane, the line-by-line Thomas algorithm is applied. Then the calculation progressed to the next plane in three-dimensional spaces to cover the whole domain. The convergence criteria were defined by the following expression:

$$\mathrm{Tol} = \frac{\sum_{k=1}^{k=K}\sum_{j=1}^{j=M}\sum_{i=1}^{i=N}|\mathrm{resid}_{ij}|}{\sum_{k=1}^{k=K}\sum_{j=1}^{j=M}\sum_{i=1}^{i=N}|\varphi_{ij}|} < 10^{-6} \tag{23}$$

4.1. Grid testing

Extensive mesh testing was performed to guarantee a grid-independent solution. Eight different meshes were used. A grid size of $110 \times 110 \times 110$ grid points (in r, θ, and z, respectively) (1 331 000 Elements) ensures a grid-independent solution and accordingly this grid was adopted in the present study.

4.2. Nusselt number calculations

The magnitude of the Nusselt number can be expressed as

$$\mathrm{Nu} = \frac{h(D)}{k} \tag{24}$$

where h and k are given by the following equations:

$$h = \frac{q''_{\mathrm{w}}}{(T_{\mathrm{w}} - T_{\mathrm{b}})} \tag{25}$$

$$k = \frac{q''_{\mathrm{w}}}{\mathrm{d}T/\mathrm{d}x} \tag{26}$$

5. RESULTS AND DISCUSSION

The current study was implemented in the heating mode using the underground temperature distributions for the month of January in four

DOI: 10.1002/er

different geographic locations in Jordan: *Salt*, *Shoubak*, *Zarqa*, and *Ghor-Safi*. The underground temperature distributions for two of these locations are shown for different months around the year in Figure 2. It is interesting to note that despite the wide seasonal variation of the surface temperature, a uniform temperature is achieved in all four locations around the year at depths beyond 40 m. However, the actual value of this uniform temperature varies from one location to another. For example, it reaches 12 and 25°C in Shoubak and Ghor Safi, respectively.

The first parameter that needs to be examined is the effect of the depth of the borehole on the outlet temperature. Figure 4 shows the variation of the outlet temperature with depth for the four locations included in the study. Although it is clear that the outlet temperature generally increases with depth, this increase becomes slower at depths beyond 50 m. This is due to the nature of the underground temperature distribution discussed earlier. Figure 4 also shows that regardless of the depth of the borehole, there is a limit to the outlet temperature that can be achieved at a given location. Consequently, successful choice of location is of extreme importance and plays a decisive role in choosing the depth of the borehole required to achieve a certain outlet temperature.

The effect of bleeding on the outlet temperature is presented in Figure 5. It compares the outlet temperature for the base case of no bleeding to that achieved with a bleed rate of 13%. This is done for 50 m deep boreholes at the four locations of interest. It is obvious that bleeding can be effectively used in all locations to increase the outlet temperature by 3–4°C and thus enhancing the overall performance of the geothermal heat pump.

The effect of bleeding and how it is affected by the properties of soil around the borehole can be examined in further detail using Figure 6. It presents the variation of outlet temperature with bleed rate for a 50 m deep borehole in *Salt* with four different values of soil porosity. This figure reveals that regardless of the soil porosity, an optimum range of bleed rate exists around

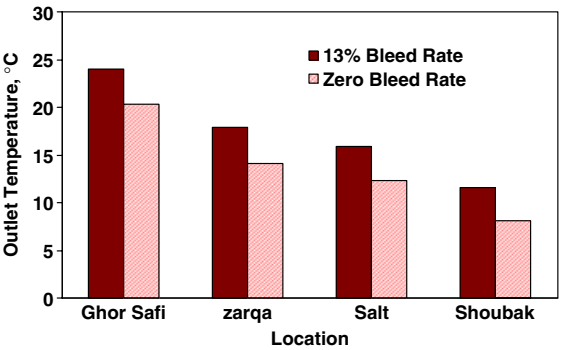

Figure 5. Variation of outlet temperature with bleed rate for four selected locations in Jordan (50 m deep borehole with 0.05 soil porosity).

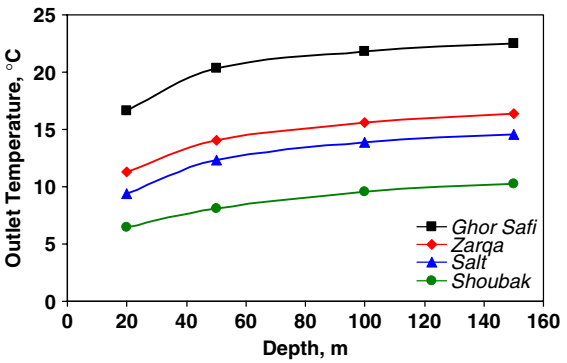

Figure 4. Variation of outlet temperature with borehole depth for four selected locations in Jordan (no bleeding and 0.05 soil porosity).

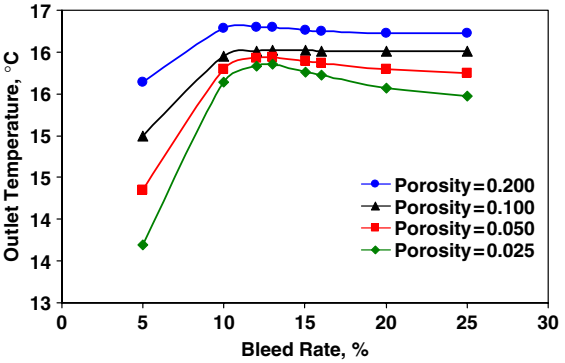

Figure 6. Variation of outlet temperature with bleed rate for various porosity values (*Salt* location and 50 m deep borehole).

DOI: 10.1002/er

12–13% which yields a maximum outlet temperature. Increasing the bleed rate beyond this range is either ineffective or even counterproductive. It can also be seen that bleeding becomes more effective in achieving higher outlet temperatures when used in locations with higher soil porosity. This can lead to the conclusion that any effective correlation for the outlet temperature should not only include the depth and the underground temperature profile, but also the bleed rate and the porosity of soil.

The results obtained from this study were compared to those published by Rees *et al.* [4]. They are presented in Figure 7, which shows a non-linear temperature distribution as a function of bleed rate. Although, the two studies use different parameters, it can be seen that a general trend exists for both studies. More importantly, both models indicate that the outlet temperature from the SCW approaches the far-field temperature as bleed rate increases. For example, the outlet temperature from the SCW for the city of *Salt* is around 16°C and the underground temperature at 50 m is approximately 17°C. This trend agrees with the results of Rees *et al.* [4], where an 11°C is obtained from their simulation with a 13.1°C far-field temperature. Thus, in a general sense both models are in agreement. Therefore, our study agrees with that of Reese *et al.* [4]. The lack of experimental data (if they exist) limits any further comparisons to be explained.

Figures 8 and 9 provide an insight into the heat transfer characteristics leading to the results obtained in Figure 6. Figure 8 shows the variation of Nusselt number in the borehole with depth for two cases: one without bleeding and the other with the optimum rate of bleeding that equals to 13%. The trend is almost identical in both cases where the Nusselt number increases sharply with depth to reach a maximum at a depth of 2–3 m and then starts decreasing until it reaches a nearly constant level at depths beyond 10 m. This can be explained by the existence of the discharge pipe outlet at a depth of 2 m which induces recirculation similar to that experienced in sudden expansion problems. As we move away from the vicinity of the pipe outlet, the recirculation effect diminishes and the

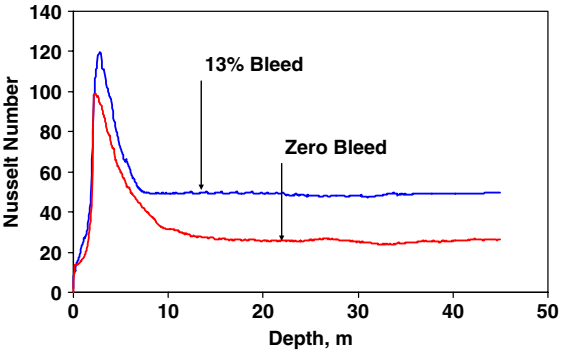

Figure 8. Variation of Nusselt number with depth for different bleed rates (*Salt* location and 0.05 soil porosity).

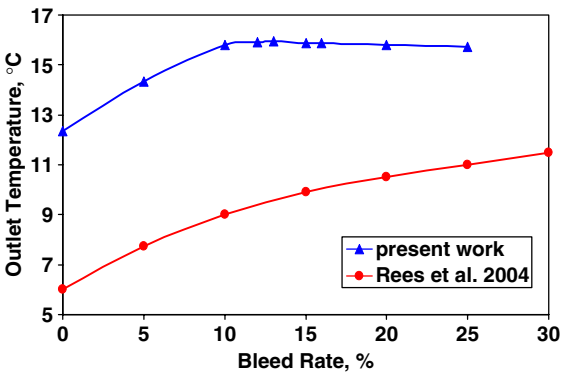

Figure 7. Variation of outlet temperature with bleed rate for *Salt* location at 0.05 porosity and 50 m deep borehole as compared with data obtained from literature.

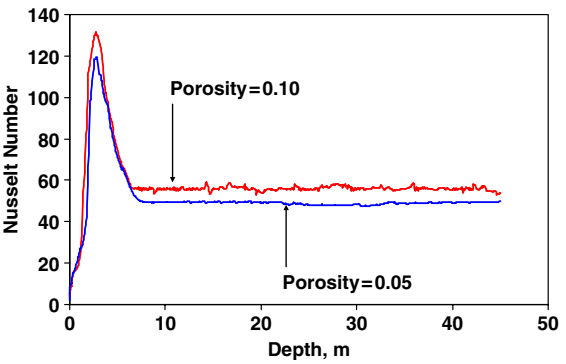

Figure 9. Variation of Nusselt number with depth for different porosity values (*Salt* location, 13% bleed rate and 0.05 soil porosity).

DOI: 10.1002/er

Nusselt number remains nearly unaffected. However, it is clear that Nusselt number increases with bleeding, especially at points deeper than 10 m where bleeding almost can double the Nusselt number. This leads to enhanced heat transfer characteristics which are reflected in the higher outlet temperatures presented in Figure 6. On the other hand, Figure 9 shows the variation of Nusselt number with depth with the bleed rate of 13% for two porosity values: 0.10 and 0.05. It is obvious that the Nusselt number increases as the porosity of the soil increases, especially beyond 10 m of depth. For example, at a depth of 20 m, a soil porosity of 0.10 results in Nusselt number 15% higher than that achieved under similar condition but with a soil porosity of 0.05.

Finally, Figure 10 addresses the justification for the three-dimensional approach employed in the current study. It shows the temperature distribution around the boundary surface of the borehole at three different depths for the base case of zero bleed rate and 0.05 soil porosity, implemented in *Salt*. It is clear that the temperature in the borehole is not only dependent on depth, but it is also a function of the angular position around the borehole. It can be seen that the temperature in the borehole increases in the vicinity of the suction pipe to reach a maximum around $\theta = 240$–270° (direction of θ as outlined in the figure), before decreasing again to a nearly uniform temperature on the opposite side of the borehole. However, this angular variation with temperature becomes less pronounced as the depth increases to reach a more uniform distribution around the borehole for depths beyond 30 m. This variation in angular temperature distribution is due to the asymmetric location of the discharge tube. Since a homogenous porous media exists, heat would have been mined uniformly if it were a symmetric borehole flow. However, since the discharge tube is closer to one end of the borehole than it is to the other end, it is creating an angular variation of temperature. At deeper depths, the discharge effects become smaller and hence the angular variation of temperature becomes damped. This result highlights the possible shortcomings of one-dimensional approaches which led to the development of the current three-dimensional model.

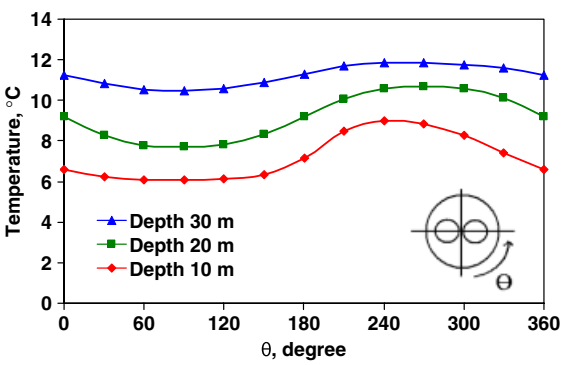

Figure 10. Temperature distribution around the borehole surface at different depths (*Salt* location, no bleeding and 0.05 soil porosity).

6. CONCLUSIONS AND RECOMMENDATIONS

A three-dimensional model was developed to analyze the performance of a SCW. This model was successfully implemented to carry out simulations of possible application in the heating mode during the month of January in four selected locations in Jordan. Simulations revealed that the outlet temperature of the SCW increases with the depth of the borehole, but this increase becomes slower at depths beyond 50 m. It was also shown that the successful choice of a location is of extreme importance since there is a limit on the outlet temperature that can be achieved at a given location.

The effect of bleeding was also thoroughly examined. It was demonstrated that although bleeding is generally effective in increasing the outlet temperature, an optimum range of bleed rate exists around 12–13% which yields a maximum outlet temperature. Increasing the bleed rate beyond this range is either ineffective or even counterproductive. It was also found that bleeding is more effective in achieving higher outlet temperatures when used in locations with higher soil porosity. These conclusions were supported by the investigation of the variation of the Nusselt number which was found to significantly increase with bleeding and higher porosities.

DOI: 10.1002/er

It was demonstrated that the temperature distribution in the borehole of the SCW is not only dependent on depth, but also on the angular position. The angular distribution of temperature around the borehole becomes nearly uniform only at depths beyond 30 m. Consequently, one-dimensional simulations need to be carried out with caution and the three-dimensional approach is better suited for performance simulation and analysis.

Finally, a number of recommendations for possible future work can be considered using the current model. For example, the effect of the mass flow rate on the outlet temperature can be examined. Also, it would be of value to study the enthalpy extracted from the standing column because this would include both the temperature and circulation rate. Moreover, a wider range of porosities and soil physical properties resulting in a wider range of permeability values and thermophysical properties can be studied. This is expected to bring about a better understanding of the significance of geographical location and soil properties on the outlet temperature and overall performance of the SCW.

NOMENCLATURE

A_d = area of discharge tube (m^2)
b = source term in the discretized from of the governing equations
C_F = Forchheimer constant = 0.143
d_p = diameter of a particle in the porous medium (m)
d_b = bleed radius (m)
D = borehole diameter (m)
h = convection heat transfer coefficient ($W\,m^{-2}\,^{\circ}C^{-1}$)
K = permeability (m^2)
l = depth from ground level (m)
L = borehole depth (m)
$\dot{m}$ = mass flow rate ($kg\,s^{-1}$)
Nu = Nusselt number
p = pressure (Pa)
q_w = heat flux ($W\,m^{-2}$)
r = radial coordinate
resid = residual
R_∞ = far away radius (m)
RU = location of the non-uniformly distributed grid around the borehole
S = source term
S_r = source term in the radial component of momentum equation
S_θ = source term in the angular component of momentum equation
S_z = source term in the axial component of momentum equation
S_T = [source term in the energy equation
t = day of the year
t_{cd} = day of the year when coldest air temperature occurs
T = temperature (°C)
T_a = temperature amplitude of air = $(T_{max} - T_{min})/2$ (°C)
T_b = bulk temperature in the borehole (°C)
T_{in} = inlet water temperature to the bore hole (°C)
T_m = mean air temperature (°C)
T_{max} = maximum air temperature (°C)
T_{min} = minimum air temperature (°C)
T_{out} = outlet temperature from the borehole (°C)
T_w = borehole wall temperature (°C)
T_∞ = faraway temperature (°C)
Tol = tolerance
u = axial velocity ($m\,s^{-1}$)
u_{in} = inlet water velocity to the borehole ($m\,s^{-1}$)
v = radial velocity ($m\,s^{-1}$)
V_b = bleed velocity at the borehole surface ($m\,s^{-1}$)
w = angular velocity ($m\,s^{-1}$)
z = axial coordinate

Greek letters

α_s = soil thermal diffusivity ($m^2\,day^{-1}$)
β = stretching constant
γ = location of grid clustering (m)
ϵ = porosity
θ = angular coordinate
μ = dynamic viscosity ($N\,s\,m^{-2}$)
ν = kinematic viscosity ($m^2\,s^{-1}$)
ρ_f = fluid density ($kg\,m^{-3}$)

DOI: 10.1002/er

Subscripts

f	= fluid inside borehole
in	= inlet
out	= outlet
s	= solid (water saturated soil)
∞	= far field

ACKNOWLEDGEMENTS

The authors would like to acknowledge 'Abdul Hameed Shoman Fund for Supporting Scientific Research' and 'The Hashemite University' for their financial supports.

REFERENCES

1. Chiasson AD, Spitler JD, Rees SJ, Smith MD. A model for simulating the performance of a shallow pond as a supplemental heat rejecter with closed-loop ground-source heat pump systems. *ASHRAE Transactions* 2000; **106**(2): 107–121.
2. Inalli M, Esen H. Experimental thermal performance evaluation of a horizontal ground-source heat pump system. *Applied Thermal Engineering* 2004; **24**:2219–2232.
3. Inalli M, Esen H. Seasonal cooling performance of a ground-coupled heat pump system in a hot and arid climate. *Renewable Energy* 2005; **30**:1411–1424.
4. Rees SJ, Spitler JD, Deng Z, Orio CD, Johnson CN. A study of geothermal heat pump and standing column well performance. *ASHRAE Transactions* 2004; **110**(1):3–13.
5. Orio CD. Geothermal heat pump applications industrial/commercial. *Energy Engineering* 1999; **96**(3):58–66.
6. Akash B, Mohsen M. Energy analysis of Jordan's urban residential sector. *Energy* 1999; **24**(9):823–831.
7. Mohsen M, Akash B. Evaluation of domestic solar water heating system in Jordan using analytic hierarchy process. *Energy Conversion and Management* 1997; **38**:1815–1822.
8. Mamlook R, Akash B, Nijmeh S. Fuzzy sets programming to perform evaluation of solar energy systems in Jordan. *Energy Conversion and Management* 2001; **42**(14):1721–1730.
9. Mohsen M, Akash B. Some prospects of energy savings in buildings. *Energy Conversion and Management* 2001; **42**(11):1307–1315.
10. Jaber J, Jaber Q, Sawalha S, Mohsen M. Evaluation of conventional and renewable energy sources for space heating in the household sector. *Renewable and Sustainable Energy Reviews* 2007; DOI: 10.1016/j.rser.2006.05.004.
11. Sunna' B. Recommended approaches to develop the direct utilization of the geothermal energy (hot water) in Jordan. *Proceedings of the International Water Demand Management Conference*, Dead Sea, Jordan, 2004.
12. Mikler V. A theoretical and experimental study of the 'energy well' performance. *Masters Thesis*, Pennsylvania State University, College Park, PA, U.S.A., 1993.
13. Yuill GK, Mikler V. Analysis of the effect of induced groundwater flow on heat transfer from a vertical open-hole concentric-tube thermal well. *ASHRAE Transactions* 1995; **101**(1):173–185.
14. Deng Z, Rees SJ, Spitler JD. A model for annual simulation of standing column well ground heat exchanger. *HVAC&R Research* 2005; **11**(4):637–655.
15. Abu-Nada E, Al-Sarkhi A, Akash B, Nijmeh S. Parametric analysis of a standing column well using a simplified one-dimensional model. *Nineteenth International Conference on Efficiency, Cost, Optimization, Simulation & Environmental Impact of Energy Systems*, Crete, Greece, 2006.
16. Akash B, Abu-Nada E, Al-Sarkhi A, Shishan A, Ibrahim A, Nijmeh S. Three-dimensional simulation of a standing column well for potential applications in Jordan. *Global Conference of Renewable Energy Approaches in Desert Regions*, Amman, Jordan, 2006.
17. White FM. *Viscous Fluid Flow*. McGraw-Hill: New York, 1991.
18. Nield DA, Bejan A. *Convection in Porous Media* (3rd edn). Springer: New York, 2006.
19. Doherty PS, Al-Huthaili S, Riffat SB, Abodahab N. Ground source heat pump-description and preliminary results of Eco House system. *Applied Thermal Engineering* 2004; **24**:2627–2641.
20. Patankar SV. *Numerical Heat Transfer and Fluid Flow*. Hemisphere, Taylor & Francis: New York, London, 1980.
21. Versteeg HK, Malalasekera W. *An Introduction to Computational Fluid Dynamic*: *The Finite Volume Method*. Wiley: New York, 1995.
22. Anderson Jr JD. *Computational Fluid Dynamics*: *The Basics with Applications*. McGraw-Hill: New York, 1995.